Journal of Mechatronics and Robotics

Original Research Paper

Real-Time Fuzzy Logic Control of Two-Link Flexible Manipulators

Jimoh Olarewaju Pedro and Juan-Paul Hynek

Department of Mechanical, Industrial and Aeronautical Engineering, University of the Witwatersrand, Johannesburg, South Africa

Article history
Received: 23-02-2023
Revised: 30-03-2023
Accepted: 31-03-2023

Corresponding Author:
Jimoh Olarewaju Pedro
Department of Mechanical, Industrial and Aeronautical Engineering, University of the Witwatersrand, Johannesburg, South Africa
Email: jimoh.pedro@wits.ac.za

Abstract: This study investigates the development of a Fuzzy Logic Controller (FLC) for tracking a sinusoidal wave trajectory and suppressing the vibration of a Two Link Flexible Manipulator (TLFM). The TLFM was modeled using Lagrange's formalism and the Assumed Mode Method (AMM). A three-part apparatus consisting of a TLFM mathematical model, a real-world TLFM, and control software was designed and implemented. The FLC was applied to both the simulated and real-world TLFM. The robustness of the FLC was investigated by considering variable payload mass and link angular velocity in both constructive and destructive link interference trajectory cases. Simulation and experimental results show the effectiveness and robustness of the proposed FLC.

Keywords: Flexible Manipulators: Fuzzy Logic Control, Vibration Suppression, Trajectory Tracking, Real-Time Experimental Simulation

Introduction

Rigid Link Manipulators (RLMs) are extensively used in various industries, typically for pick-and-place and assembly line operations (Zebin and Alam, 2012). However, Flexible Link Manipulators (FLMs) are becoming a popular alternative to RLMs due to their lightweight, high speed, and lower operating costs. These factors make them more attractive in many applications. For example, the lightweight construction of a manipulator is essential in the aerospace industry, as it makes it cost-effective and safer to operate. On the other hand, FLMs are inherently highly nonlinear and distributed, underactuated systems with non-collocated actuators and sensors. As a result, they often require robust closed-loop control to overcome these issues (Tokhi and Azad, 2008).

Designing, manufacturing, and implementing FLM test facilities are time-consuming and expensive. Therefore, a more suitable platform is desired for implementing and experimentally validating different control schemes. Mathematical models of FLMs, implemented in simulation environments have the potential to satisfy this need. Single-link FLMs lack the intricacies of multi-link FLMs, so a planar TLFM that captures the coupling between the rigid and flexible motions of the elbow and shoulder links is considered. The dynamics of FLMs are typically viewed as the superposition of rigid bodies and flexible dynamics. Due to the well-developed kinematics approach to controlling rigid manipulators, convention dictates that flexible dynamics are addressed independently. To this end, vibration control strategies developed for these and other applications are implemented. There are two vibration control strategies for FLMs: Passive and active (Tokhi and Azad, 2008). Passive control adjusts the physical properties of the FLM to reduce the complexity of the control problem. It can dampen high vibrational modes less effectively handled by active control. However, passive control alone cannot eliminate the large amplitude deflections, which must be dealt with using active methods (Subedi *et al*., 2020; Lochan *et al*., 2016; Kiang *et al*., 2015; Tokhi and Azad, 2008; Saragih and Mahardhika, 2009).

Various control schemes have been successfully implemented for multi-link FLMs to address their transient behavior and coupled parameters (Alandoli and Lee, 2020; Subedi *et al*., 2020; Lochan *et al*., 2016; Kiang *et al*., 2015; Sayahkarajy *et al*., 2016). include: Proportional Integral Derivative (PID) (Pedro and Tshabalala, 2015; Mallikarjunaiah and Reddy, 2013; Mahamood and Pedro, 2011; Tokhi and Azad, 2008); linear state feedback, adaptive (Qiu *et al*., 2019; Chu and Cui, 2015; Pradhan and Subudhi, 2012; Feliu *et al*., 2006); computed torque (Wang and Hou, 2018; Sawada and Itamiya, 2012; Li *et al*., 2021); singular perturbation analysis (Wang *et al*., 2014; Khorrami, 1989; Li *et al*., 2021); frequency domain analysis; Linear Quadratic Regulator (LQR)

Science Publications

© 2023 Jimoh Olarewaju Pedro and Juan-Paul Hynek. This open-access article is distributed under a Creative Commons Attribution (CC-BY) 4.0 license.

DOI: 10.3844/jmrsp.2023.48.62

(Khairudin *et al*., 2011; Alandoli *et al*., 2021); Sliding Mode Control (SMC) (Kherraz *et al*., 2014; Lochan *et al*., 2015; Wang and Sun, 2014; Mamani *et al*., 2012); back stepping control (Yang *et al*., 2015; Zouari *et al*., 2013); Model Predictive Control (MPC) (Elliott *et al*., 2014; Silva *et al*., 2020); fuzzy logic-based (Pradhan and Subudhi, 2013; Li *et al*., 2013; Sarkhel *et al*., 2020; Kasruddin Nasir *et al*., 2022; Green and Sasiadek, 2005; Alandoli *et al*., 2021); evolutionary algorithm-based (Rahimi and Nazemizadeh, 2014; Zain *et al*., 2009); adaptive neural network-based control (Pedro and Tshabalala, 2015; Jiang, 2015; Al-Assadi *et al*., 2011; Yan and Wang, 2012; Rahmani and Belkheiri, 2019; Gao *et al*., 2018); and hybrid neuro-fuzzy control (Qiu *et al*., 2019; Antony, 2019; Kharabian and Mirinejad, 2020; Alandoli and Lee, 2020; Khan and Kara, 2020). The following terms were used during the publication search: “Two-link flexible robotic manipulator", "control of a flexible-link manipulator”, “flexible-link robotic manipulator vibration suppression”, “fuzzy logic control” and “flexible-link robotic manipulator trajectory tracking”.

LQR is a control technique that utilizes a state-space approach to analyze a system. This technique is based on the idea of transferring the designer's iterations on pole location, as used in state feedback, to iterations on the elements in some cost function J concerning the state x and control u subject to the constraint $\dot{x}$ given state for all $x \in R^n$ (Khairudin *et al*., 2011; Alandoli *et al*., 2017). On the other hand, SMC consists of a two-step procedure. The first step is to describe the control objective in terms of a state space surface, namely the sliding surface. This surface choice must be developed such that the system trajectories satisfy the performance specifications when the sliding variable lies on the sliding surface. The second step, controller design, is represented by the definition of a control action that steers the state trajectories onto the sliding surface after a finite transient time (Kherraz *et al*., 2014; Lochan *et al*., 2015; Wang and Sun, 2014; Mamani *et al*., 2012; Gao and Lu, 2022).

Fuzzy Logic Control (FLC) is a linguistic-based control scheme that incorporates human-like characteristics within a controller. This type of controller is rooted in the vagueness surrounding the classification of inputs (Lochan *et al*., 2016; Abdullahi *et al*., 2013; Pradhan and Subudhi, 2013; Li *et al*., 2013; Kasruddin Nasir *et al*., 2022; Ponce-Cruz and Ramírez-Figueroa, 2010; Alandoli *et al*., 2021). Neural Networks (NNs), conversely, mimic the way the brain works, with their architecture primarily determined by the connections between elements. Because of this, NNs, along with fuzzy logic, are considered artificial intelligence. NNs can be trained to perform a specific function by adjusting the values of the connecting weights between elements (Pedro and Tshabalala, 2015; Jiang, 2015; Al-Assadi *et al*., 2011; Yan and Wang, 2012; Rahmani and Belkheiri, 2019). Hybrid neuro-fuzzy controllers consist of two significant parts: The NN controller, followed by the FLC. While NNs on their own can be challenging to understand because the variables lack meaning, they are often combined with fuzzy logic, producing a more intuitive approach for operators and controller designers (Qiu *et al*., 2019; Antony, 2019; Kharabian and Mirinejad, 2020; Alandoli and Lee, 2020; Khan and Kara, 2020; Tinkir *et al*., 2010).

FLCs are becoming increasingly popular due to their ease of use and modification by system operators. Sayahkarajy *et al*. (2016); Lochan *et al*. (2016) provide a comprehensive review of the control of TLFMs, noting FLC as capable of controlling TLFMs. However, most experiments are simulation-based, thus necessitating additional real-time experimentation and validation. The premise of this study is to experimentally validate direct adaptive Mamdani-type FLCs for vibration suppression and trajectory tracking (Pradhan and Subudhi, 2013; Li *et al*., 2013; Kasruddin Nasir *et al*., 2022). The controllers are designed directly based on the fuzzy rule base to satisfy the control objectives. In this study, the Mamdani fuzzy logic control technique and its implementation for the TLFM control will be discussed in detail (Behera and Kar, 2010). The choice of the Mamdani fuzzy inference system is motivated by its ability to provide good results with a relatively simple structure and interpretable rule base. It is also characterized by its expressive power, i.e., its unique ability to simultaneously use numerical and verbal data from human knowledge and experience and easy formalization (Fahmy and Zaher 2015).

The paper makes significant contributions in three areas: Firstly, it verifies and validates the mathematical model for predicting the dynamics of a TLFM; secondly, it designs and validates direct adaptive Mamdani-type FLCs for both trajectory tracking and vibration suppression of the nonlinear, complex, and underactuated TLFM test rig; and finally provides a detailed analysis of the proposed controller's robustness to payload variations and modeling errors arising from the inclusion of actuator dynamics.

System Mathematical Modelling

The mathematical model of the TLFM is derived using Euler-Lagrange and the assumed modes methods (Subudhi and Pradhan, 2016; Khairudin *et al*., 2010; Lee and Alandoli, 2020; Subedi *et al*., 2021). The Assumed Modes Method (AMM) entails vibration analysis of the flexible links such that modes and natural frequencies are assumed and the deflection thereof is superimposed with the deflection due to the inertia of the payload (Nguyen and Morris, 2007). The AMM has been successfully used in describing the dynamics

DOI: 10.3844/jmrsp.2023.48.62

associated with the TLFMs (De Luca and Siciliano, 1991; Zebin and Alam, 2012). Using AMM to produce a closed-form equation describing the TLFM is error-prone due to the fact the number of modes is assumed. Thus, a modal analysis using Finite Element Method (FEM) is conducted on the links to determine the predominant modes of vibration and the frequencies thereof. To describe the dynamics of a TLFM, it is first necessary to derive the general expression for an n-link Flexible Manipulator (FM). Figure 1 shows the local and global reference frames used in the derivation of the equations of motion.

The coordinate reference frames used include the global reference frame, denoted by the axes (X_0, Y_0), the local link reference frame, denoted by the axes (X_i, Y_i), and the local flexible link reference frame, denoted by axes $\left(\hat{X}_i, \hat{Y}_i\right)$.

Equation 1 shows the transformation matrix relating the rotation of the (X_{i+1}, Y_{i+1}) axis to that of the (X_i, Y_i) axis:

$$A_i = \begin{bmatrix} \cos\theta_i & -\sin\theta_i \\ \sin\theta_i & \cos\theta_i \end{bmatrix} \tag{1}$$

where, $\theta_i \approx 0^o$ (Lochan *et al*., 2016) $\frac{\partial v_i(x_i,t)}{\partial x_i}$ is the slope, and $v_i(x_i, t)$ is the bending deflection at any point x_i and time t along the i^{th} link.

The elastic homogeneous transformation matrix, E_i, is given by Eq. 2:

$$E_i = \begin{bmatrix} 1 & -\frac{\partial v_i(x_i,t)}{\partial x_i} \\ \left.\frac{\partial v_i(x_i,t)}{\partial x_i}\right|_{x_i=l_i} & 1 \end{bmatrix} \tag{2}$$

where, l_i are the length of the i^{th} link. Let $r_i^i(x_i) = \begin{Bmatrix} x_i \\ v_i(x_i,t) \end{Bmatrix}$ a position vector on the i^{th} link with respect to the (X_i, Y_i) reference frame and the same position vector with respect to the (X_0, Y_0) reference frame be denoted as r_i^0. The position of the origin of the (X_{i+1}, Y_{i+1}) reference frame with respect to the (X_i, Y_i) reference frame may thus be expressed as:

$$p_{i+1}^i = r_i^i(l_i) \tag{3}$$

where, p_{i+1}^i is evaluated at $x_i = l_i$ in Eq. 3. The position of the origin of the (X_{i+1}, Y_{i+1}) reference frame with respect to the (X_0, Y_0) reference frame is denoted as p_i^0.

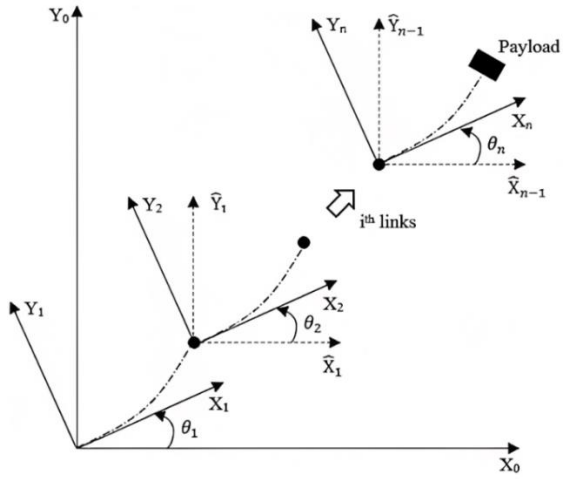

Fig. 1: Structure of an N-link flexible manipulator reference frames

The global transformation matrix, shown in Eq. 4, relates the reference frames (X_0, Y_0) and (X_i, Y_i):

$$T_i = T_{i-1} A_i \tag{4}$$

where, $T_0 = I$ and I is an identity matrix of size 2 × 2. In Eqs. 5-6 the global transformation matrices are used to express any position vector r_i^0 on the i^{th} link as well as the position of the $(i+1)^{th}$ link origin with respect to the (X_0, Y_0):

$$r_i^0 = p_i^0 + T_i\, r_i^i \tag{5}$$

and:

$$p_{i+1}^0 = p_i^0 + T_i\, p_{i+1}^i \tag{6}$$

The general form of the Euler-Lagrange equation denoted by Eq. 7, considers both the kinetic and potential energies of the system:

$$\frac{d}{dt}\left(\frac{\partial L}{\partial \dot{q}_k}\right) - \frac{\partial L}{\partial q_k} + \frac{\partial D}{\partial \dot{q}_k} = F_i \tag{7}$$

where, Lagrangian $L = T - V$ and T and V are the total kinetic and potential energies of the system, respectively. F_i is the torque vector associated with the hub motors. D is the Rayleigh's dissipation function. The total kinetic energy of the manipulator is given by Eq. 8:

$$T = T_R + T_L + T_{PL} \tag{8}$$

where, T_R is the kinetic energy of the hubs, T_L is the kinetic energy of the links and T_{PL} is the kinetic energy of the payload. Shown in Eq. 9 is the kinetic energy of the i^{th} hub:

$$T_R = \frac{1}{2} J_i \dot{\theta}_i^2 \tag{9}$$

DOI: 10.3844/jmrsp.2023.48.62

where, J_i is the moment of inertia of the hub about the i^{th} hub axis and $\dot{\theta}_i$ is the angular velocity associated with the i^{th} link about the hub axis. Equation 10 is the total kinetic energy for n-hubs:

$$T_R = \frac{1}{2}\dot{\theta}^T J \dot{\theta} \tag{10}$$

where, $\dot{\theta} = \left[\dot{\theta}_1, \dot{\theta}_2, ...\dot{\theta}_n\right]$ and J = diagonal [J_1, J_2,...,J_n]. Expressed in Eq. 11 is the link kinetic energy:

$$T_{Li} = \frac{1}{2}\rho_i \int_0^{l_i} \left(\dot{r}_i^0\right)^T \dot{r}_i \, dx_i \tag{11}$$

where:

$$\dot{r}_i^0 = \dot{p}_i^0 + \dot{T}_i \, r_i^i + T_i \, \dot{r}_i^i \tag{12}$$

ρ_i is the mass per unit length. The term $\dot{r}_i^0$ in Eq. 12 is a result of differentiating Eq. 5. $\dot{p}_i^0$ is determined by differentiating Eqs. 3 and 6, thus expressing $\dot{p}_i^0$ in terms of $\dot{p}_{i+1}^0$, T_i, $\dot{T}_i$, $\dot{r}_i^i$ (l_i), and r_i^i (l_i). The derivative of the global transformation matrix is recursively calculated and is shown to be:

$$\dot{T}_i = \dot{\tilde{T}}_{i+1} A_i + \tilde{T}_{i+1} \dot{A}_i \tag{13}$$

In Eq. 13, $\dot{\tilde{T}}_i = T_i \, E_i + T_i \, \dot{E}_i$, in which $\dot{E}_i S = \frac{\partial v_i(x_i, t)}{\partial x_i}$. S is defined as the sign matrix having the following entries $\begin{bmatrix} 0 & -1 \\ 1 & 0 \end{bmatrix}$ and $\dot{A}_i = S A_i \theta_i$. The transpose of Eq. 12 is evaluated using matrix identities. Summing Eq. 11 over the number of links results in the total kinetic energy shown in Eq. 14:

$$T_L = \sum_{i=1}^{N} \frac{1}{2} p_i \int_0^{l_i} \left(\dot{r}_i^0\right)^T \dot{r}_i \, dx_i \tag{14}$$

Payload dynamics is necessary, particularly in cases where the endpoint has significant mass, which may change. The kinetic energy associated with the payload is given by Eq. 15:

$$T_{PL} \frac{1}{2} M_p \, \dot{p}_{n+1}^T \dot{p}_{n+1} + \frac{1}{2} Ip\left(\dot{\varphi}_n + \dot{v}_n^{'}\right)^2 \tag{15}$$

where, $\dot{\varphi}_n = \sum_{j=1}^{n} \theta_j + \sum_{k=1}^{n-1} \dot{v}_k'$ and n is the number of links. The term $\dot{v}'_n$ is evaluated at $x_i = l_i$ and the prime indicator means differentiated with respect to x_i. M_P and I_P are the point mass and inertia of the payload, respectively. The total kinetic energy is computed by summing Eqs. 10-15.

The potential energy of the links expressed in Eq. 16 neglects the effects of gravity (planar motion) and considers only rigid joints:

$$V = \sum_{i=1}^{n} \frac{1}{2} \int_0^{l_i} (EI) i \left(\frac{d^2 v_i(x_i)}{dx_i^2}\right) dx_i \tag{16}$$

where, $(EI)_i$ is the flexural rigidity of the system. In Eq. 7, Rayleigh's dissipation function for all links is given in matrix form by Eq. 17:

$$D = \frac{1}{2} \dot{q}^T C \dot{q}^T \tag{17}$$

where matrix C is a diagonal damping matrix consisting of damping coefficients, where the number of rows is equal to n and the number of columns is equal to n_m (number of modes). Vector q is the modal displacement vector. The deflection of the links is expressed by superimposing Eq. 18 with vibration analysis:

$$(EI)_i \frac{\partial^4 v_i(x_i, t)}{\partial x_i^4} + \rho i \frac{\partial^2 v_i(xi, t)}{\partial t^2} = 0 \tag{18}$$

The typical form of Euler-Bernoulli's beam theory is given in Eq. 18. The following cantilever beam boundary conditions are considered:

$$v_i = 0 \, at \, x_i = 0, i.e., deflection \, is \, zero \, at \, a \, fixed \, location$$

$$\frac{dv_i}{dx_i} = 0 \, at \, x_i = 0, i.e., The \, slop \, is \, zero \, at \, a \, fixed \, location$$

Equations 19-20 describe the relationship between shear force, bending moment, and deflection. In the case of a flexible manipulator, the $V(x)$ and $M(x)$ terms are replaced with equivalent shear force and bending moment terms that account for the link mass, payload mass, and distal link masses, as in Eqs. 21-22:

$$EI \frac{d^3 v}{dx^3} = V(x) \tag{19}$$

$$EI \frac{d^2 v}{dx^2} = M(x) \tag{20}$$

DOI: 10.3844/jmrsp.2023.48.62

Hence Eqs. 21-22:

$$(EI)_i \left.\frac{\partial^2 v_i(x_i,t)}{\partial x_i^2}\right|_{x_i=l_i} = I_{E_i}\frac{d^2}{dt^2}\left(\left.\frac{\partial v_i(x_i,t)}{\partial x_i}\right|_{x_i=l_i}\right) - M_{DE_i}\frac{d^2}{dt^2}\left(v_i(x_i,t)\middle|x_i=l_i\right) \quad (21)$$

$$(EI)_i \left.\frac{\partial^3 v_i(x_i,t)}{\partial x_i^3}\right|_{x_i=l_i} = M_{E_i}\frac{\partial^2}{\partial t^2}\left(v_i(x_i,t)\middle|x_i=l_i\right) + M_{DE_i}\frac{d^2}{dt^2}\left(\left.\frac{\partial v_i(x_i,t)}{\partial x_i}\right|_{x_i=l_i}\right) \quad (22)$$

where, M_{Ei} and I_{Ei} are the effective mass and inertia associated with the i^{th} link, whilst M_{DEi} is the effective equivalent mass of the distal links concentrated at the end of the i^{th} link. The expressions are:

$$M_{Ei} = \frac{M_{Li}}{m_i},\ I_{Ei} = \frac{I_{Li}}{m_i l_i},\ and\ M_{DEi} = \frac{M_{Di}}{m_i l_i^2}$$

The variables m_i, M_{Li}, I_{Li}, and M_{Di} are the individual link mass, link mass expression, link inertia expression, and distal link mass expression, respectively. The approximate deflection of a continuous beam, under vibratory conditions (different modes), is given by Eq. 23:

$$v_i(x_i,t) = \sum_{i=1}^{nm} \gamma ij(x_i)\, qij(t) \quad (23)$$

where, $\gamma_{ij}(x_i)$ is the mode shape function (j = 1,2,..., n), related to the i^{th} link and $q_{ij}(t)$ is the modal displacement for the i^{th} link based on the j^{th} mode shape. Combining Eqs. 18 and 23 yields Eq. 24:

$$\frac{(EI)_i}{\rho_i \gamma ij(x_i)}\frac{d^4 \gamma ij(x_i)}{dx_i^4} = -\frac{1}{qij(t)}\frac{d^2 qij(t)}{dt^2} \quad (24)$$

The term $-\frac{1}{qij(t)}\frac{d^2 qij(t)}{dt^2}$ is a constant equivalent to the natural frequency squared at the given j^{th} mode of vibration (ω_{ij}^2). Thus, rearranging Eq. 24 into temporal and spatial components gives Eqs. 25 and 26:

$$\frac{d^2\left[(EI)_i\, d^2 \gamma ij(x_i)\right]}{dx_i^2} - \omega_{ij}^2 \rho_i\, \gamma ij(x_i) = 0 \quad (25)$$

$$\frac{d^2 qij(t)}{dt^2} + \omega_{ij}^2 qij(t) = 0 \quad (26)$$

From Eq. 26, the second-order homogeneous differential equation of the form $\ddot{y} + a\dot{y} + by = 0$ is solved to give the expression for q_{ij} in Eq. 27:

$$qij(t) = e^{\omega ijt} \quad (27)$$

To solve for the mode shape function, consider Eq. 25 and apply the general 4th order homogeneous differential equation solution. Solving for the constants using the cantilever boundary conditions results in Eq. 28, noting the expression for $\gamma_{ij}(x_i)$ as:

$$\gamma ij = N_{ij}\left[\cos(\beta_{ij}x_i) - \cosh(\beta_{ij}x_i) + \delta_{ij}\sinh(\beta_{ij}) - \cosh(\beta_{ij}x_i)\right] \quad (28)$$

where the normalizing mode shape constant, N_{ij}, is equivalent to m_i and δ_{ij} is given by Eq. 29:

$$\delta_{ij} = \frac{\sin\beta_{ij} - \sinh\beta_{ij} + M_{Ei}\beta_{ij}\left(\cos\beta_{ij} - \cosh\beta_{ij}\right) - M_{DEi}\beta_{ij}^2\left(\sin\beta_{ij} + \sinh\beta_{ij}\right)}{\cos\beta_{ij} + \cosh\beta_{ij} - M_{Ei}\beta_{il}\left(\sin\beta_{ij} + \sinh\beta_{ij}\right) - M_{DEi}\beta_{ij}^2\left(\cos\beta_{ij} - \cosh\beta_{ij}\right)} \quad (29)$$

and β_{ij} is solved using numerical methods and expressed in Eq. 30:

$$\begin{aligned} &1+\cosh\beta_{ij}l_i\cos\beta_{ij}l_i - M_{Ei}\beta_{ij}\left(\sinh\beta_{ij}l_i - -\cosh\beta_{ij}l_i\cos\beta_{ij}l_i\right) \\ &-I_{Ei}\beta_{ij}^3 l_i\left(\sinh\beta_{ij}+\cosh\beta_{ij}l_i\sin\beta_{ij}l_i - 1\right) + M_{DEi}^2\beta_{ij}^4 \\ &\left(1-\cosh\beta_{ij}l_i\sin\beta_{ij}l_i\right) - 2M_{DEi}^2\beta_{ij}^4\sinh\beta_{ij}l_i = 0 \end{aligned} \quad (30)$$

Calculating the natural frequency of the i^{th} link with regard to the j^{th} mode shape is required to describe the deflections associated with any point along each flexible link. Equation 31 is used to solve for the natural frequency:

$$\beta_{ij}^4 = \frac{\omega_{ij}^2 \rho_i}{(EI)_i} \quad (31)$$

Considering only two flexible links, the superposition of the deflections in Eqs. 18 and 23, yields the total deflection at any position x_i, which when combined with Euler-Lagrange energy equations, results in the closed-form expression in Eq. 32 (Subedi *et al*., 2021):

$$M\ddot{q} + D\dot{q} + Kq + h(\dot{q},q) = \tau \quad (32)$$

where, M is the positive, symmetric inertia matrix, D is the damping matrix, K is the link stiffness matrix and τ is the torque vector. The h vector is defined in Eq. 33 using Christoffel symbols:

$$h_i = \sum_{j=1}^{n+m_d}\sum_{k=1}^{n+m_d}\left(\frac{\partial \gamma_{ij}}{\partial q_k} - \frac{1}{2}\frac{\partial \beta_{jk}}{\partial q_i}\right)\dot{q}_j\dot{q}_k \quad (33)$$

DOI: 10.3844/jmrsp.2023.48.62

The link stiffness matrix is given by Eq. 34:

$$K = diag\left\{0 \;\; 0 \;\; \omega_{11}^2 m_1 \;\; \omega_{12}^2 m_1 \;\; \omega_{21}^2 m_2 \;\; \omega_{22}^2 m_2\right\} \quad (34)$$

and the damping matrix is given by Eq.35:

$$D = diag\left\{0 \;\; 0 \;\; 0.1\sqrt{\omega_{11}^2 m_1} \;\; 0.1\sqrt{\omega_{12}^2 m_1} \;\; 0.1\sqrt{\omega_{21}^2 m_2} \;\; 0.1\sqrt{\omega_{22}^2 m_2}\right\} \quad (35)$$

For mathematical modeling purposes, both the shoulder and elbow actuators' dynamics were unspecified, thus using the MATLAB system identification toolbox, transfer functions describing the dynamics were approximated from the real-time input-output data. The transfer functions describe the relationship between the given in Eqs. 36-37

Elbow:

$$\frac{V(S)}{\dot{\theta}(S)} = \frac{-28.19s + 6.526}{s^2 + 9.281 \times 10^{-9} s + 1.707} \quad (36)$$

Shoulder:

voltage ($V(s)$) and the angular velocity $\left(\dot{\theta}(s)\right)$ are:

$$\frac{V(S)}{\dot{\theta}(S)} = \frac{-0.01663s^4 - 2.321s^3 - 259.9s^2 - 1.784\times10^{-4}s - 4.206\times10^{-4}}{s^4 + 78.98s^3 + 1617s + 1519} \quad (37)$$

The flexible link properties and servo drive settings are given in Tables 1-2, respectively. In Table 1, link 1 refers to the link closest to the base, whilst in Table 2, servo drive 1 refers to the shoulder motor drive.

Controller Implementation

Figure 2 shows the general form of a PD-like direct adaptive Mamdani-type FLC architecture, where the setpoint together with the negative feedback produces an error, *e*. The error is an input to the FLC, where it is then fuzzified, rules are inferred and the fuzzy value produced is defuzified to crisp control output. To reduce jerking, the derivative of the error is also an input to the FLC (Subedi *et al*., 2020; Sayahkarajy *et al*., 2016). The FLC input-output membership functions may take many different forms, with the most common being triangular and spanning the controller operating range (Gao and He, 2016). Mamdani-type FLCs have an IF antecedent, then consequent rule-base structure (Jantzen, 2013), where the antecedent and consequent are both fuzzy sets. This property defines Mamdani-type FLCs. Using the input membership functions, the rule base, and the output membership functions, a fuzzy value is produced. The fuzzy value is defuzzified to control output, typically by means of the center of gravity method (Jantzen, 2013). Unlike Takagi-Sugeno fuzzy logic, explicit system identification is not needed for controller design when using the Mamdani fuzzy logic inference engine (Behera and Kar, 2010).

The main goal of the controllers is to track a generated desired input $y_d = [\theta_{1d}, \theta_{2d}, \varepsilon_{1d}, \varepsilon_{2d}]^T$, where θ_{1d} and θ_{2d} are the desired hubs' angles, respectively; and ε_{1d} and ε_{2d} are the endpoint deflections (strains).

Table 1: Geometric and material parameters of the flexible links

Links	Width (mm)	Length (mm)	Height (mm)	Material
Link 1	2.0	330	40	304 stainless steel
Link 2	0.9	330	40	304 stainless steel

Table 2: Settings of the servo drives

Servo drives	η_{max} (%)	I ×R (%)	Offset (%)	I_{max} (%)	Gain (%)
1	100	0	50	100	10
2	100	0	50	25	15

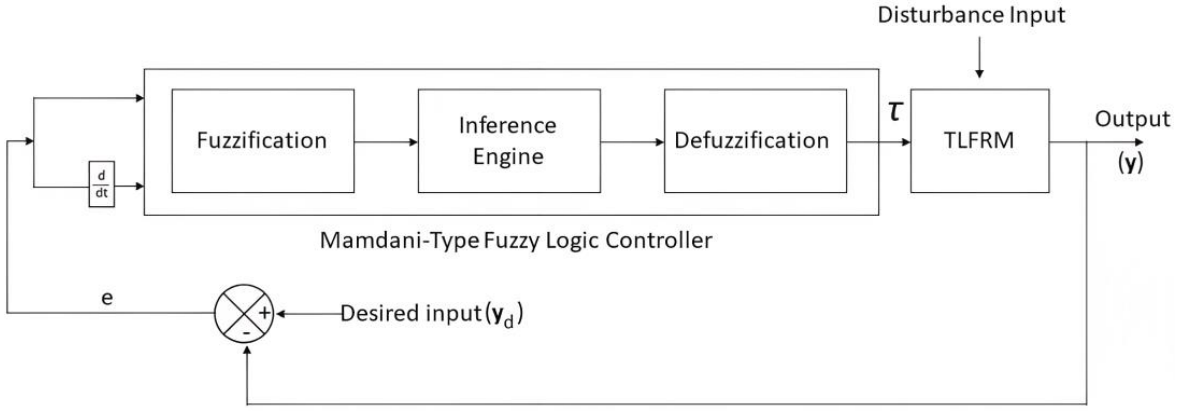

Fig. 2: PD-like direct adaptive mamdani-type FLC

DOI: 10.3844/jmrsp.2023.48.62

The performance index to be minimized by the designed controllers is shown in Eq. 38:

$$J=\frac{1}{T}\int_0^T\left[\sum_{I=1}^{2}\left(\frac{e_i}{e_{i_{\max}}}\right)^2+\left(\frac{\varepsilon_i}{\varepsilon_{i_{\max}}}\right)^2+\left(\frac{\tau_i}{\tau_{i_{\max}}}\right)^2\right]dt \quad (38)$$

where, T is the final run time; $e_i = \theta_{id}-\theta_i$ is the tracking error; $e_{i_{\max}}$ $(\theta_{id}-\theta_i)_{\max}$ is the strain; $\varepsilon_{i_{\max}}$ is the expected maximum strain; τ_i is the control torque; and $\tau_{i_{\max}}$ is the maximum torque that the actuator can produce. The desired input is given by Eq. 39:

$$y_d=\begin{bmatrix}\theta_{1_d}=\theta_{d_{\max}}\sin 2\pi ft\\ \theta_{2_d}=\theta_{d_{\max}}\sin(2\pi ft+\pi)\\ \varepsilon_{1_d}=0\\ \varepsilon_{2_d}=0\end{bmatrix} \quad (39)$$

where, $\theta_{d_{\max}}$ and f are the amplitude and frequency of the sine wave for the desired hub angle, respectively. $\varepsilon_{1d} = \varepsilon_{1d} = 0$ because, in addition to trajectory tracking, we are also concerned with vibration suppression. PD-like Mamdani fuzzy logic controllers were developed for each of the controlled Degrees of Freedom (DoF), i.e., trajectory tracking and vibration suppression. The input to each of the controllers was the state error and the time rate of change of the state error. Figure 2 shows the implemented FLC architecture.

Real-Time Trajectory Tracking

The inputs to the trajectory tracking FLC are the tracking error and the time rate of change of the tracking error. The closed-loop PD and PID input-output data is used to obtain the primary closed-loop observation of the TLFM dynamic behavior. This gave the operational closed loop ranges of the tracking error and its corresponding time rate of change. This information was used as an initial knowledge base. Once the initial knowledge base had been established, membership functions for the controller input and output variables had to be developed.

The trajectory tracking input and output membership functions are shown in Figs. 3-4, respectively. Similarly to (Zebin and Alam, 2012), the membership functions selected are predominantly triangular. There are two inputs and two outputs associated with the trajectory tracking FLC. The trajectory tracking FLC inputs are the errors due to the difference between the set point trajectory and the actual trajectory, whilst the outputs are the motor-supplied voltages, with the corresponding servo drive settings in Table 2.

The trajectory tracking FLC inputs are classified into five fuzzy sets, namely negative and positive strong, negative and positive weak, and median. These sets are centrally clustered such that the trajectory tracking FLC sensitivity is increased and the stability is decreased. The input ranges are: -120° ≤ x ≤120°, where the inputs are saturated when x ≤ -10° and x ≥10°. Similarly, the trajectory tracking FLC outputs are classified into five fuzzy sets, namely fast Anticlockwise (A-C), fast Clockwise (C), medium A-C, medium C, and slow/no. The output ranges are: -4 $V \leq x \leq 4$ V and -4.4 $V \leq x \leq 4.4$ V, respectively, where the latter refers to the shoulder actuator. Note that the central trapezoidal output membership function for both the trajectory tracking FLC outputs accounts for the dead zone in the actuators. The trajectory tracking FLC rule base consists of ten rules, each consisting of one antecedent and one consequent. Tables 3-4 show the rules. Note that the numbers in each element of the tables refer to the rule number, where in Table 3, NS = Negative Strong, NW = Negative Weak, M = Median, PW = Positive Weak, and PS = Positive Strong, and in Table 4, where A-C = anticlockwise and C = Clockwise.

Figure 5 shows the fuzzy surface with the saturation-like relationship between the elbow angle error input and the elbow motor-supplied voltage output. Thus, a small angle error results in a large control output. This is true for the relationship between the shoulder angle error input and the shoulder motor-supplied voltage output as well.

Real-time Vibration Suppression

The vibration suppression input and output membership functions are shown in Figs. 6-7, respectively. There are six inputs and two outputs associated with the vibration suppression FLC. The vibration suppression FLC inputs are the errors due to the difference between the set point strain of zero and the actual strain. Like the trajectory tracking FLC, the vibration suppression FLC outputs are the motor-supplied voltages. The vibration suppression FLC inputs are classified into five fuzzy sets, namely negative strong, positive strong, negative weak, positive weak, and median. The input ranges are -0.6 $V \leq x \leq 0.6$ V, -3 $V \leq x \leq 3$ V, -0.8 $V \leq x \leq 0.8$ V, -0.8 $V \leq x \leq 0.8$ V, -1.4 $V \leq x \leq 1.4$ V and -3 $V \leq x \leq 3$ V respectively, progressing in the order from the strain gauge closest to the payload.

Table 3: Trajectory tracking FLC antecedents

Link angles	NS	NW	M	PW	PS
Elbow	1	2	3	5	4
Shoulder	6	7	8	9	10

Table 4: Trajectory tracking FLC consequents

Motor voltages	Fast A-C	Medium A-C	Slow/ No	Medium C	Fast C
Tip	1	2	3	5	4
Base	6	7	8	10	9

DOI: 10.3844/jmrsp.2023.48.62

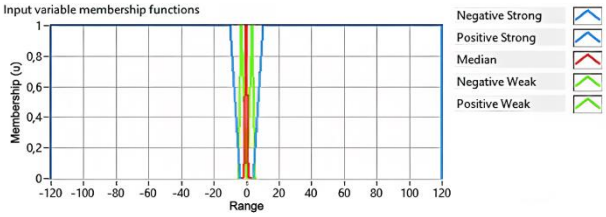

Fig. 3: Trajectory tracking FLC input membership

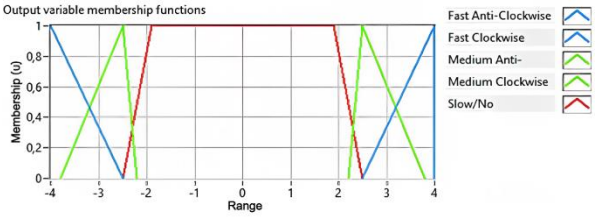

Fig. 4: Trajectory tracking FLC output membership functions

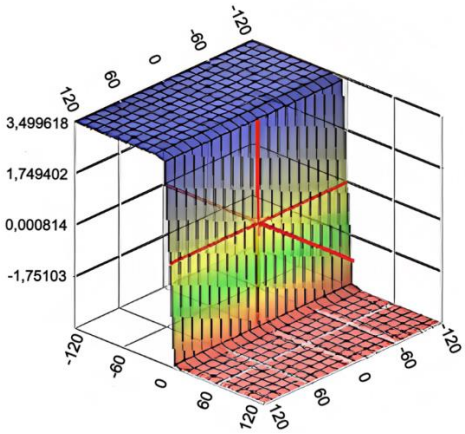

Fig. 5: Trajectory tracking FLC fuzzy surface

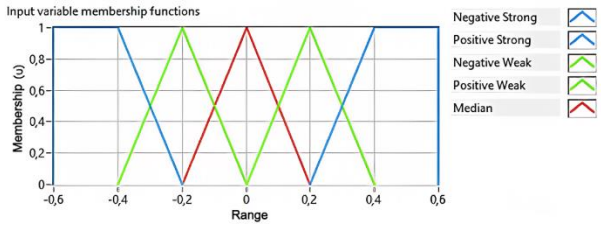

Fig. 6: Vibration suppression FLC input membership functions

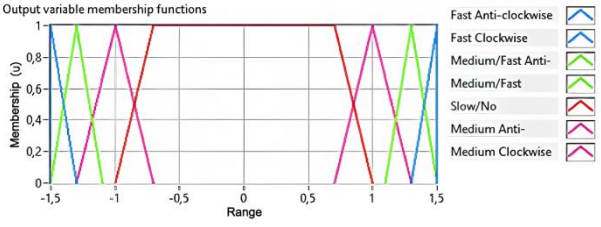

Fig. 7: Vibration suppression FLC output membership

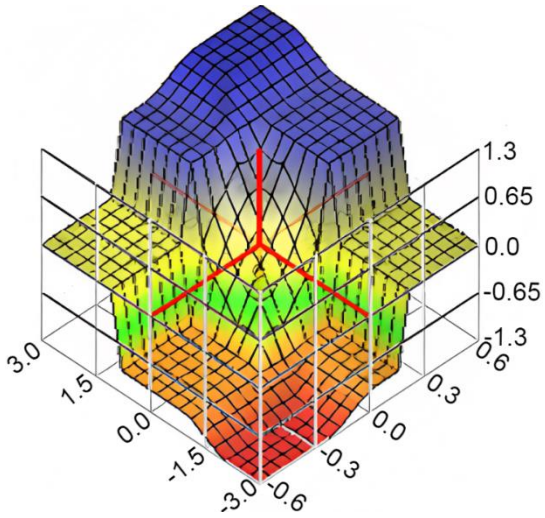

Fig. 8: Vibration suppression FLC fuzzy surface

The vibration suppression FLC outputs are classified into seven fuzzy sets, namely fast Anticlockwise (A-C), fast Clockwise (C), medium/fast Anticlockwise (A-C), medium/fast Clockwise (C), slow/no, medium Anticlockwise (A-C) and medium clockwise (C). The vibration suppression FLC output ranges are -1.5 V $\leq x \leq$ 1.5 *V* and -3.5 *V* $\leq x \leq$ 3.5 *V*, respectively, where the latter refers to the shoulder actuator.

The vibration suppression FLC rule base consists of one hundred and one rules, each consisting of three antecedents and one consequent. Tables 5-6 give the rules. The tables are symmetrical and the first three strains are considered for the tip link, whilst the next three strains are for the base link. This reduces the number of rules and since the links are inherently coupled through the strains, this may be done. Note that NS = Negative Strong, NW = Negative Weak, M = Median, PS = Positive Strong, and PW = Positive Weak.

Figure 8 shows the fuzzy surface with the relationship between the first strain error and the elbow motor supplied voltage output. Figure 14 shows that a peak/trough strain error behavior exists. There are four peaks and four troughs, each pair representing a quarter cycle. A peak corresponding to the maximum strain error of 2,25 *V* occurs at *t* = 2s and corresponds to a strain that is a result of the flexible link being momentarily stationary at the turning point and, due to inertial drag, starts experiencing increased strain as the link progresses from the turning point to *t* = 2s.

Experimental Facilities

Like in Khairudin *et al*. (2011); Subudhi and Pradhan (2016), the real-time TLFM test rig consists of two flexible links connected in series and actuated both at the shoulder and elbow joints by means of armature-controlled DC motors. The motors are 12 V, 0.59 nm, and 24 V, 1 nm, with the latter being the shoulder actuator. The reason

DOI: 10.3844/jmrsp.2023.48.62

the actuators have different load ratings is due to the respective load that either actuator is expected to carry (rotate). Both motors are driven by separate 24 V DC servo drives and power supply combinations. Collocated and non-collocated feedback is achieved by means of two incremental encoders, one at each joint, and six full-bridge strain gauges, three on each link. The incremental encoders have 500 pulses per revolution and the strain gauges are rated 120 Ω. Feedback from the incremental encoders is used for trajectory tracking, while feedback from the strain gauges is used for vibration suppression. Due to the millivolt output from the strain gauges, a six-channel strain gauge amplifier is used with a gain of 1000 to amplify the strain signals before acquisition. The real-time data acquisition and transmission are achieved by means of a NI PCI6221 (68-pin) data-acquisition card slotted into a real-time target PC and coupled with an SCB-68 terminal box. A NI PCI8232 ethernet card is used for serial communication between the host PC and the real-time target PC. The real-time target route was chosen for the deterministic processing of data.

Table 5: Vibration suppression FLC antecedents

	NS	NW	M	PW	PS
Strain 1 error	1, 2, 3, 4, 5, 6, 7, 8, 9	10, 11, 12, 13, 14, 15, 16, 17, 18	19, 20, 21, 22, 23, 24, 25, 26, 27, 46, 47, 48, 49, 51, 52, 53	37, 38, 39, 40, 41, 42, 43, 44, 45	28, 29, 30, 31, 32, 33, 34, 35, 36
Strain 2 error	1, 2, 3, 10, 11, 12, 19, 20, 21	4, 5, 6, 13, 14, 15, 22, 23, 24	7, 8, 9, 16, 17, 18, 25, 26, 27, 34, 35, 36, 43, 44, 45, 52, 53	31, 32, 33, 40, 41, 42, 49, 50, 51	28, 29, 30, 37, 38, 39, 46, 47, 48
Strain 3 error	1, 4, 7, 10, 13, 16, 19, 22, 25	2, 5, 8, 11, 14, 17, 20, 23, 26	3, 6, 9, 12, 15, 18, 21, 24, 27, 30, 33, 36, 39, 42, 45, 48, 51	29, 32, 35, 38, 41, 44, 47, 50, 53	28, 31, 34, 37, 40, 43, 46, 49, 52
Strain 4 error	54, 55, 56, 57, 58, 59, 60, 61, 62	63, 64, 65, 66, 67, 68, 69, 70, 71	72, 73, 74, 75, 76, 77, 78, 79, 80, 99, 100, 101, 102, 103, 104, 105, 106	90, 91, 92, 93, 94, 95, 96, 97, 98	81, 82, 83, 84, 85, 86, 87, 88, 89
Strain 5 error	54, 55, 56, 63, 64, 65, 72, 73, 74	57, 58, 59, 66, 67, 68, 75, 76, 77	60, 61, 62, 69, 70, 71, 78, 79, 80, 87, 88, 89, 96, 97, 98, 105, 106	84, 85, 86, 93, 94, 95, 102, 103, 104	81, 82, 83, 90, 91, 92, 99, 100, 101
Strain 6 error	54, 57, 60, 63, 66, 69, 72, 75, 78	55, 58, 61, 64, 67, 70, 73, 76, 79	56, 59, 62, 65, 68, 71, 74, 77, 80, 83, 86, 89, 92, 95, 98, 101, 104	82, 85, 87, 88, 91, 94, 97, 100, 103, 106	81, 84, 87, 90, 93, 96, 99, 102, 105

Table 6: Vibration suppression FLC consequents

	Fast anticlockwise clockwise	Medium/fast anticlockwise	Medium	Slow no	Medium clockwise	Medium/fast	Fast
Tip motor voltage	1, 2, 3, 4, 10	3, 5, 7, 11, 12, 13, 19	6, 8, 9, 14, 15, 16, 17, 18, 20, 21, 22, 23, 24, 25, 26	27	33, 35, 36, 41, 42, 43, 44, 45, 47, 48, 49, 50, 51, 52, 53	30, 32, 34, 38, 39, 40, 46	28, 29, 31, 37
Base motor voltage	54, 55, 57, 63	56, 58, 60, 64, 65, 66, 72	59, 61, 62, 67, 68, 69, 70, 71, 73, 74, 75, 76, 77, 78, 79	80	86, 88, 89, 94, 95, 96, 98, 100, 102, 103, 104, 105, 106	83, 85, 87, 91, 92, 93, 99	81, 82, 84, 90

DOI: 10.3844/jmrsp.2023.48.62

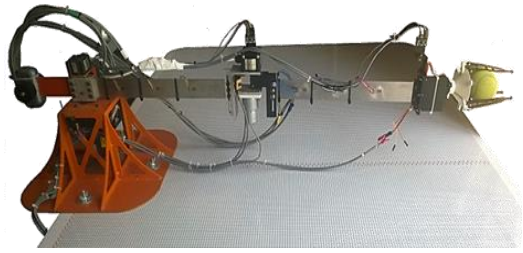

Fig. 9: Two-link flexible manipulator test rig

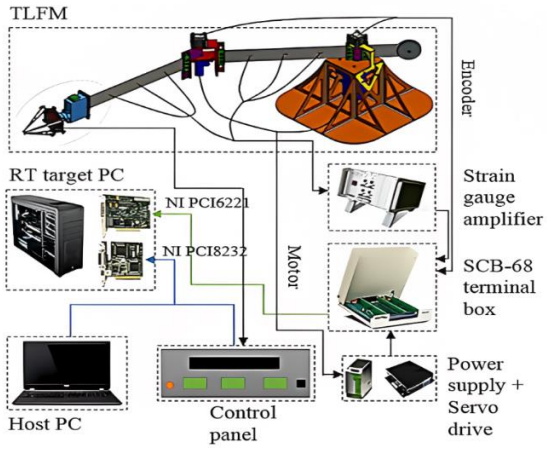

Fig. 10: Layout of the two-link flexible manipulator

The control software was developed in LabVIEW and deployed from the host PC to the real-time target PC. To control the TLFM without the necessity of a host PC, an Arduino-based control panel was constructed, which would relay user input to the real-time target PC. Additionally, a trajectory tracking table supported the base of the TLFM such that the incremental encoder outputs may be verified and calibrated visually. Figure 9 shows the designed experimental test rig for the TLFM.

An accelerometer and gyro meter combination were mounted on the tip of each link (Fig. 9). This provides an alternative form of deflection feedback and may substitute or be used in conjunction with the strain gauges for vibration suppression. The end effector/gripper has a mass of 180 g without payload, whereas with payload, the total mass is 280 g. The layout of the TLFM is shown in Fig. 10.

Results and Discussion

Numerical Simulations

Performing a modal Finite Element Analysis (FEA) on both flexible links (Table 1 for the geometrical parameters of the links) yielded the conclusion that the first two modes of vibration were the most dominant. Thus, using Eq. 34 and considering only two modes of vibration for each link, the mathematical model block diagram was constructed in LabVIEW control and simulation environment. Coupled with actuator dynamics, the mathematical model allowed for the preliminary development of both trajectory tracking and vibration suppression FLCs. The FEA results are presented in Fig. 11 and Table 7.

Sinusoidal trajectory tracking is investigated in this study since it reflects common repetitive back-and-forth applications. As such, the actual trajectory of both links in a constructive interference case is shown in Fig. 12. Both cases in Figs. 12-13 are conducted at 0.2 cycles per second (cps) with a 100 g payload. Figure 13 shows the results of a destructive interference case, where destructive interference refers to the trajectories of both links being out of phase by 180.

Figure 15 shows that the destructive test case resulted in a more uniform strain error. The oscillatory behavior from Fig. 14 was mitigated. Both the average and absolute maximum strain errors were significantly reduced by introducing destructive link interference.

To construct robust trajectory tracking and vibration suppression FLCs, sixty-four test cases were considered.

The test cases were limited to a maximum angular velocity of 0.2 cycles per second and a trajectory tracking amplitude of 60°. The test cases considered are presented in Table 8.

Table 7: Flexible link dominant modes of vibration

Links	Mode 1 frequency (Hz)	Mode 2 frequency (Hz)
1	15.72	98.98
2	7.09	44.66

Table 8: Cases analyzed for the FLCs' robustness

Cases
A-30° base and tip, 0° phase
B-30° base and tip, 180° phase
C-30° base and tip, 0° phase
D-30° base and tip, 180° phase
E-30° base and tip, 0° phase
F-30° base and tip, 180° phase
G-30° base and tip, 0° phase
H-30° base and tip, 180° phase
I-x = 500 mm, y = 600 mm
J-x = -500 mm, y = 600 mm
K-x = 600 mm, y = 500 mm
L-x = -600 mm, y = 500 mm
M-60° base and tip, 0° phase
N-60° base and tip, 180° phase
O-0° base and 60° tip, 0° phase
P-45° base and 0° tip, 0° phase

Fig. 11: ANSYS FEA modal deflection analysis for the TLFM link

DOI: 10.3844/jmrsp.2023.48.62

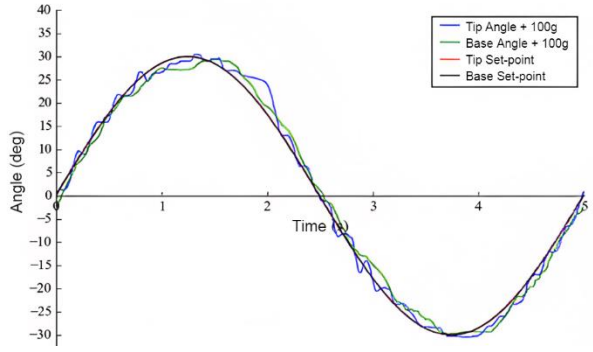

Fig. 12: Sinusoidal trajectory tracking of amplitude 30° and 0.2 cycles per second by the FLC constructive interference with payload

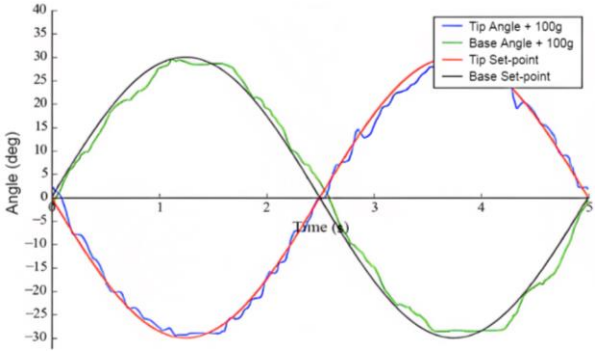

Fig. 13: Sinusoidal trajectory tracking of amplitude 30° and 0.2 cycles per second by the FLC destructive interference with payload

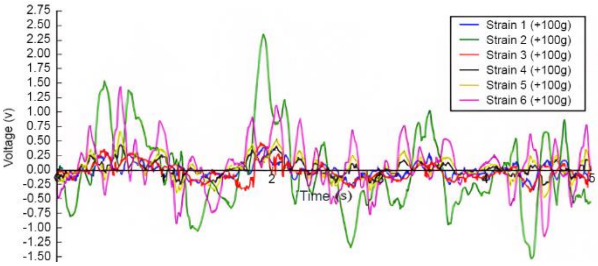

Fig. 14: Vibration suppression for sinusoidal trajectory tracking of amplitude 30° and 0.2 cycles per second by the FLC constructive interference with payload

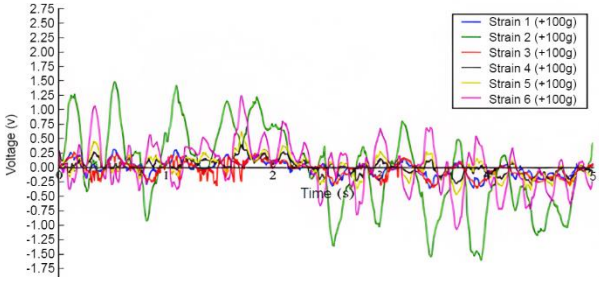

Fig. 15: Vibration suppression for sinusoidal trajectory tracking of amplitude 30° and 0.2 cycles per second by the FLC destructive interference with payload

Figures 16-17 show the trajectory tracking results related to sixteen of the test cases. Cases E, G, and O yield the least error in both trajectory tracking and vibration suppression, thus, are preferential cases. From Figs. 16-17, it is seen that the average angle error is increased for a payload of 100 g. This is due to the increased inertia. Both the average and absolute maximum strain errors are comparable to data in the published literature. Test cases *M* and *N* are the worst cases, as the increased distance results in a system response that is too slow.

Figures 18-19 show the FLC control outputs corresponding to Figs. 12 and 16. Figure 18 is the control provided by the trajectory tracking FLC, whilst Fig. 19 is the control provided by the vibration suppression FLC. The shoulder actuator control voltage is larger due to the size of the shoulder actuator. The oscillatory behavior in Fig. 14 is the opposite and repeated in the vibration suppression control action in Fig. 19.

The mathematical model proved that it sufficiently approximates the real-time test rig in that only minor tuning modifications was made for adaptation. From Figs. 12-13, the introduction of destructive link interference resulted in a reduction in trajectory tracking angle error in both links. This is justifiable, considering that the angular momentum of either flexible link effectively acts against one another in a destructive case. This was, however, not true throughout all the test cases, as seen from Figs. 16-17.

Considering the fact that the average and absolute maximum trajectory tracking and vibration suppression errors were roughly similar for each 0° phase-180° phase pair means that the trajectory tracking and vibration suppression FLCs display a degree of robustness. The introduction of a payload resulted in both the average and absolute maximum angle and strain error increasing slightly. This is in line with the increased system inertia. Figures 14-15 show that the maximum strain errors occur just after or before a turning point. This can be attributed to the acceleration and deceleration of the flexible links.

The introduction of destructive interference results in less strain error when comparing Figs. 14-15. Similar to trajectory tracking, this is due to the inertial cancellation of the flexible links. The largest strain errors induced on each link are representative of the common mode of vibration that the links are experiencing. The tip link predominantly vibrated in the second mode of vibration, whilst the base link vibrated predominantly in the first mode of vibration. The best test cases, in Figs. 16-17, represent single-link motions. This may be due in part to the systematic tuning of the FLCs; however, it may also be attributed to the reduction in link motions occurring.

The worst case occurred when tracking a 60° amplitude sinusoidal trajectory. This case was followed by the user input test cases, where *x* and *y* coordinates

DOI: 10.3844/jmrsp.2023.48.62

were specified. The trajectory tracking angle errors of the user input cases are due to large start-up torque requirements as well as the conflicting behavior between the trajectory tracking and vibration suppression FLCs. The conflicting behavior between both controllers occurs due to the opposite in rotation control outputs. This was mitigated by applying gains to both controllers' outputs, making the trajectory tracking FLC more dominant, and by applying delays in the control software looping structure. The conflicting controller behavior is shown in Figs. 18-19, where at a given time *t*, the control outputs may be opposite in sign. The use of triangular membership functions for both inputs and outputs aided in cheap computing. Figure 18, the saturation-like trajectory tracking FLC resulted in control outputs that plateaued. This induced slight jerking in the base link, however, was necessary such that the limits of the actuators were not exceeded. The results of the test cases are shown in Figs. 16-17, were conducted with a payload and at 0.2 cycles per second. From these results, the maximum average angle error was 3.2°, whilst the maximum absolute angle error was 9.8°. Although the maximum absolute angle error is observably high, it made sense considering the system's capabilities. Hence showing that *N* and *M* test cases represent the threshold of effective control for the proposed FLCs. The maximum average strain error was 1.2 V, whilst the maximum absolute strain error was 3.1 V.

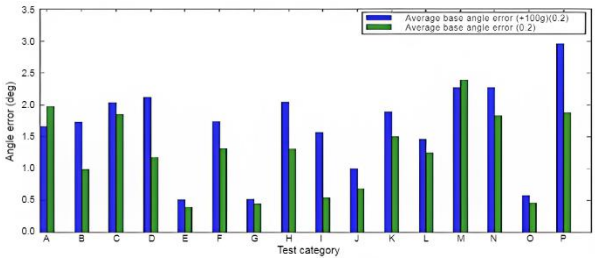

Fig. 16: Base average angle error, 0.2 cycles per second with payload

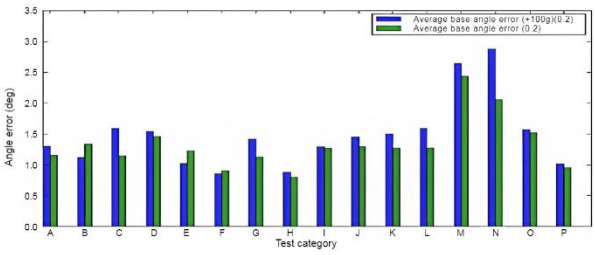

Fig. 17: Tip average angle error, 0.2 cycles per second with payload

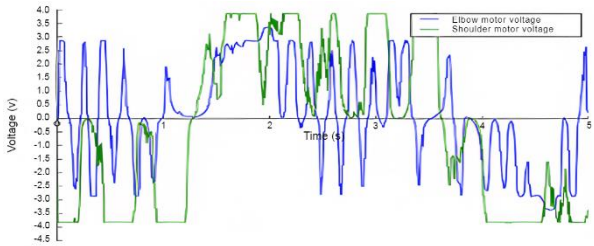

Fig. 18: Control outputs for sinusoidal trajectory tracking of amplitude 30° and 0.2 cycles per second by the FLC constructive interference with payload

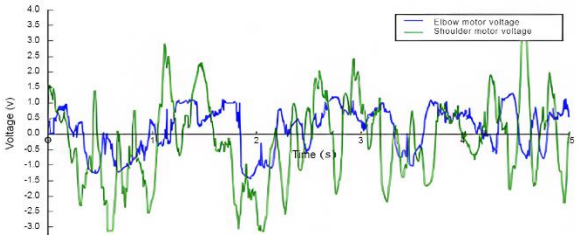

Fig. 19: Control outputs for vibration suppression during sinusoidal trajectory tracking of amplitude 30° and 0.2 cycles per second by the FLC constructive interference with payload

Conclusion

The mathematical model allowed for the sufficient development of the preliminary FLCs. Deviations from the mathematical model were mostly attributed to the actuator dynamics approximations. The proposed FLCs for both trajectory tracking and vibration suppression showed good robustness qualities, disturbance rejection, and noise attenuation. Destructive link interference is preferred since it generally reduces the angle and strain errors. Future work will involve the applications of different types of single-objective and multi-objective optimization algorithms to tune the proposed FLCs gains and their associated membership functions.

Acknowledgment

The authors would like to thank the University of the Witwatersrand, Johannesburg, South Africa, for their assistance and support.

Funding Information

The authors should acknowledge the funders of this manuscript and provide all necessary funding information.

Author's Contributions

Jimoh Olarewaju Pedro: Developed the research conceptualization, problem formulation, and research methodology and also organized the research project and supervision.

Juan-Paul Hynek: Designed the direct adaptive Mamdani-type fuzzy logic controllers for both the trajectory tracking and vibration suppression of the nonlinear, complex, and underactuated two-link flexible manipulator. Designed and built the test rig used for experimental validation.

Ethics

This article is original and contains unpublished material. The corresponding author confirms that the second author has read and approved the manuscript. The authors declare that there are no ethical issues and no conflict of interest that may arise after the publication of this manuscript.

References

Abdullahi, A. M., Mohamed, Z., & Muhammad, M. (2013). A Pd-Type fuzzy logic control approach for vibration control of a single-link flexible manipulator. *International Journal of Research in Engineering and Science*, *1*(4), 37-47. https://doi.org/10.5121/ijics.2013.3402

Al-Assadi, H. M. A. A., Mat Isa, A. A., Hasan, A. T., Rahman, Z. A., & Heimann, B. (2011). Development of a real-time-position prediction algorithm for under-actuated robot manipulator by using of artificial neural network. *Proceedings of the Institution of Mechanical Engineers, Part C: Journal of Mechanical Engineering Science*, *225*(8), 1991-1998. https://doi.org/10.1177/0954406211400345

Alandoli, E. A., Rashid, M. Z. A., & Sulaiman, M. (2017). A Comparison of Pid And Lqr Controllers For Position Tracking and Vibration Suppression of Flexible Link Manipulator. *Journal of Theoretical & Applied Information Technology*, *95*(13).

Alandoli, E. A., & Lee, T. S. (2020). A critical review of control techniques for flexible and rigid link manipulators. *Robotica*, *38*(12), 2239-2265. https://doi.org/10.1017/S0263574720000223

Alandoli, E. A., Lee, T. S., Lin, Y. J., & Vijayakumar, V. (2021). Dynamic model and intelligent optimal controller of flexible link manipulator system with payload uncertainty. *Arabian Journal for Science and Engineering*, *46*, 7423-7433. https://doi.org/10.1007/s13369-021-05436-7

Antony, J. (2019). Position Control of a Single Link Flexible Joint Robot Manipulator using Adaptive Neuro-Fuzzy Control System. *Irish Interdisciplinary Journal of Science & Research (IIJSR), (Quarterly International Journal) Volume*, *3*, 58-66.

Behera, L., & Kar, I. (2010). *Intelligent systems and control principles and applications*. Oxford University Press, Inc.

Chu, Z., & Cui, J. (2015). Experiment on vibration control of a two-link flexible manipulator using an input shaper and adaptive positive position feedback. *Advances in Mechanical Engineering*, *7*(10), https://doi.org/10.1177/1687814015610466

De Luca, A., & Siciliano, B. (1991). Closed-form dynamic model of planar multilink lightweight robots. *IEEE Transactions on Systems, Man and Cybernetics*, *21*(4), 826-839. https://doi.org/10.1109/21.108300

Elliott, J. R., Dubay, R., Mohany, A., & Hassan, M. (2014). Model predictive control of vibration in a two flexible link manipulator-part 2. *Journal of Low Frequency Noise, Vibration and Active Control*, *33*(4), 469-483. https://doi.org/10.1260/0263-0923.33.4.469

Fahmy, R., & Zaher, H. (2015). A comparison between fuzzy inference systems for prediction (with application to prices of fund in Egypt). *International Journal of Computer Applications*, *109*(13). https://doi.org/10.5120/19246-0604

Feliu, V., Pereira, E., Diaz, I. M., & Roncero, P. (2006). Feedforward control of multimode single-link flexible manipulators based on an optimal mechanical design. *Robotics and Autonomous Systems*, *54*(8), 651-666. https://doi.org/10.1016/j.robot.2006.02.012

Gao, H., & He, W. (2016, November). Fuzzy control of a single-link flexible robotic manipulator using assumed mode method. In *2016 31st Youth Academic Annual Conference of Chinese Association of Automation (YAC)* (pp. 201-206). IEEE. https://doi.org/10.1109/YAC.2016.7804889

Gao, H., He, W., Zhou, C., & Sun, C. (2018). Neural network control of a two-link flexible robotic manipulator using assumed mode method. *IEEE Transactions on Industrial Informatics*, *15*(2), 755-765. https://doi.org/10.1109/TII.2018.2818120

Gao, Y., & Lu, H. (2022). Sliding Mode Control of Flexible Articulated Manipulator Based on Robust Observer. *Computational Intelligence and Neuroscience*, *2022*. https://doi.org/10.1155/2022/2440770

Green, A., & Sasiadek, J. Z. (2005). Adaptive control of a flexible robot using fuzzy logic. *Journal of Guidance, Control and Dynamics*, *28*(1), 36-42. https://doi.org/10.2514/1.6376

Jantzen, J. (2013). *Foundations of fuzzy control: A practical approach*. John Wiley & Sons. https://doi.org/10.1002/9781118535608

Jiang, Z. H. (2015, May). Workspace trajectory control of flexible robot manipulators using neural network and visual sensor feedback. In *2015 IEEE 28th Canadian Conference on Electrical and Computer Engineering (CCECE)* (pp. 1502-1507). IEEE. https://doi.org/10.1109/CCECE.2015.7129503

Kasruddin Nasir, A. N., Ahmad, M. A., & Tokhi, M. O. (2022). Hybrid spiral-bacterial foraging algorithm for a fuzzy control design of a flexible manipulator. *Journal of Low Frequency Noise, Vibration and Active Control*, *41*(1), 340-358. https://doi.org/10.1177/14613484211035646

Khairudin, M., Mohamed, Z., Husain, A. R., & Ahmad, M. A. (2010). Dynamic modelling and characterisation of a two-link flexible robot manipulator. *Journal of Low Frequency Noise, Vibration and Active Control*, *29*(3), 207-219. https://doi.org/10.1260/0263-0923.29.3.207

Khairudin, M., Mohamed, Z., & Husain, A. R. (2011). Dynamic model and robust control of flexible link robot manipulator. *Telkomnika (Telecommunication Computing Electronics and Control)*, *9*(2), 279-286. https://doi.org/10.12928/telkomnika.v9i2.698

Khan, M. U., & Kara, T. (2020). Adaptive control of a two-link flexible manipulator using a type-2 neural fuzzy system. *Arabian Journal for Science and Engineering*, *45*(3), 1949-1960. https://doi.org/10.1007/s13369-020-04341-9

Kharabian, B., & Mirinejad, H. (2020). Hybrid sliding mode/H-infinity control approach for uncertain flexible manipulators. *IEEE Access*, *8*, 170452-170460. https://doi.org/10.1109/ACCESS.2020.3024150

Kherraz, K., Hamerlain, M., & Achour, N. (2014, December). Robust sliding mode controller for a class of under-actuated systems. In *2014 15th International Conference on Sciences and Techniques of Automatic Control and Computer Engineering (STA)* (pp. 942-946). IEEE. https://doi.org/10.1109/STA.2014.7086751

Khorrami, F. (1989, December). Analysis of multi-link flexible manipulators via asymptotic expansions. In *Proceedings of the 28th IEEE Conference on Decision and Control*, (pp. 2089-2094). IEEE.

Kiang, C. T., Spowage, A., & Yoong, C. K. (2015). Review of control and sensor system of flexible manipulator. *Journal of Intelligent & Robotic Systems*, *77*, 187-213. https://doi.org/10.1007/s10846-014-0071-4

Lee, T. S., & Alandoli, E. A. (2020). A critical review of modelling methods for flexible and rigid link manipulators. *Journal of the Brazilian Society of Mechanical Sciences and Engineering*, *42*, 1-14. https://doi.org/10.1007/s40430-020-02602-0

Li, K., Wang, H., Liang, X., & Miao, Y. (2021). Visual servoing of flexible-link manipulators by considering vibration suppression without deformation measurements. *IEEE Transactions on Cybernetics*, *52*(11), 12454-12463. https://doi.org/10.1109/ TCYB.2021.3072779

Li, Y., Tong, S., & Li, T. (2013). Adaptive fuzzy output feedback control for a single-link flexible robot manipulator driven DC motor via backstepping. *Nonlinear Analysis: Real World Applications*, *14*(1), 483-494. https://doi.org/10.1016/j.nonrwa.2012.07.010

Lochan, K., Roy, B. K., & Subudhi, B. (2016). A review on two-link flexible manipulators. *Annual Reviews in Control*, *42*, 346-367. https://doi.org/10.1016/j.arcontrol.2016.09.019

Lochan, K., Suklabaidya, S., & Roy, B. K. (2015, July). Sliding mode and adaptive sliding mode control approaches of two-link flexible manipulator. In *Proceedings of the 2015 Conference on Advances in Robotics* (pp. 1-6). https://doi.org/10.1145/2783449.2783508

Mahamood, R. M., & Pedro, J. O. (2011, May). Hybrid PD/PID controller design for two-link flexible manipulators. In *2011 8th Asian Control Conference (ASCC)*, (pp. 1358-1363). IEEE.

Mallikarjunaiah, S., & Reddy, S. N. (2013). Design of pid controller for flexible link manipulator. *International Journal of Engineering Research and Applications*, *3*(6), 1207-1212.

Mamani, G., Becedas, J., & Feliu, V. (2012). Sliding mode tracking control of a very lightweight single-link flexible robot robust to payload changes and motor friction. *Journal of Vibration and Control*, *18*(8), 1141-1155. https://doi.org/10.1177/1077546311416269

Nguyen, V. B., & Morris, A. S. (2007). Genetic algorithm tuned fuzzy logic controller for a robot arm with two-link flexibility and two-joint elasticity. *Journal of Intelligent and Robotic Systems*, *49*, 3-18. https://doi.org/10.1007/s10846-006-9097-6

Pedro, J. O., & Tshabalala, T. (2015, May). Hybrid NNMPC/PID control of a two-link flexible manipulator with actuator dynamics. In *2015 10th Asian Control Conference (ASCC)* (pp. 1-6). IEEE. https://doi.org/10.1109/ASCC.2015.7244737

Ponce-Cruz, P., & Ramírez-Figueroa, F. D. (2010). *Intelligent control for LabVIEW*, (pp. 1-8). Springer London. https://doi.org/10.1007/978-1-84882-684-7_1

Pradhan, S. K., & Subudhi, B. (2012). Real-time adaptive control of a flexible manipulator using reinforcement learning. *IEEE Transactions on Automation Science and Engineering*, *9*(2), 237-249. https://doi.org/10.1109/TASE.2012.2189004

Pradhan, S. K., & Subudhi, B. (2013, August). Fuzzy learning based adaptive control for a two-link flexible manipulator. In *2013 IEEE International Conference on Control Applications (CCA)*, (pp. 282-287). IEEE. https://doi.org/10.1109/CCA.2013.6662772

Qiu, Z. C., Li, C., & Zhang, X. M. (2019). Experimental study on active vibration control for a kind of two-link flexible manipulator. *Mechanical Systems and Signal Processing*, *118*, 623-644. https://doi.org/10.1016/j.ymssp.2018.09.001

Rahimi, H. N., & Nazemizadeh, M. (2014). Dynamic analysis and intelligent control techniques for flexible manipulators: A review. *Advanced Robotics*, *28*(2), 63-76. https://doi.org/10.1080/01691864.2013.839079

Rahmani, B., & Belkheiri, M. (2019). Adaptive neural network output feedback control for flexible multi-link robotic manipulators. *International Journal of Control*, *92*(10), 2324-2338. https://doi.org/10.1080/00207179.2018.1436774

Saragih, R., & Mahardhika, T. (2009, December). Design of passive control for flexible structure using genetic algorithm. In *2009 IEEE International Conference on Control and Automation*, (pp. 2249-2253). IEEE. https://doi.org/10.1109/ICCA.2009.5410416

Sarkhel, P., Banerjee, N., & Hui, N. B. (2020). Fuzzy logic-based tuning of PID controller to control flexible manipulators. *SN Applied Sciences*, *2*, 1-11. https://doi.org/10.1007/s42452-020-2877-y

Sawada, M., & Itamiya, K. (2012, September). A position control of 2 DOF flexible link robot arms based on computed torque method. In *The 2012 International Conference on Advanced Mechatronic Systems*, (pp. 547-552). IEEE.

Sayahkarajy, M., Mohamed, Z., & Mohd Faudzi, A. A. (2016). Review of modelling and control of flexible-link manipulators. *Proceedings of the Institution of Mechanical Engineers, Part I: Journal of Systems and Control Engineering*, *230*(8), 861-873. https://doi. org/10.1177/0959651816642099

Silva, B. P., Santana, B. A., Santos, T. L., & Martins, M. A. (2020). An implementable stabilizing model predictive controller applied to a rotary flexible link: An experimental case study. *Control Engineering Practice*, *99*, 104396. https://doi.org/10.1016/j.conengprac.2020.104396

Subedi, D., Tyapin, I., & Hovland, G. (2020). Review on modeling and control of flexible link manipulators. *Modeling, Identification and Control*, *41*(3), 141-163, https://doi.org/10.4173/mic.2020.3.2

Subedi, D., Tyapin, I., & Hovland, G. (2021). Dynamic modeling of planar multi-link flexible manipulators. *Robotics*, *10*(2), 70. https://doi.org/10.3390/robotics10020070

Subudhi, B., & Pradhan, S. K. (2016). A flexible robotic control experiment for teaching nonlinear adaptive control. *International Journal of Electrical Engineering Education*, *53*(4), 341-356. https://doi.org/10.1177/0020720916631159

Tinkir, M., Önen, Ü., & Kalyoncu, M. (2010). Modelling of neurofuzzy control of a flexible link. *Proceedings of the Institution of Mechanical Engineers, Part I: Journal of Systems and Control Engineering*, *224*(5), 529-543. https://doi.org/10.1243/09596518JSCE785

Tokhi, M. O., & Azad, A. K. (Eds.). (2008). *Flexible robot manipulators: Modelling, Simulation and Control*, (Vol. *68*). Iet. https://doi.org/10.1049/PBCE068E

Wang, X., & Hou, B. (2018). Trajectory tracking control of a 2-DOF manipulator using computed torque control combined with an implicit lyapunov function method. *Journal of Mechanical Science and Technology*, *32*, 2803-2816. https://doi.org/10.1007/s12206-018-0537-6

Wang, Y., Han, F., Feng, Y., & Xia, H. (2014, October). Hybrid continuous nonsingular terminal sliding mode control of uncertain flexible manipulators. In *IECON 2014-40th Annual Conference of the IEEE Industrial Electronics Society*, (pp. 190-196). IEEE. https://doi.org/10.1109/IMCCC.2014.74

Wang, Y., & Sun, L. (2014, September). On the optimized continuous nonsingular terminal sliding mode control of flexible manipulators. In *2014 4th International Conference on Instrumentation and Measurement, Computer, Communication and Control*, (pp. 324-329). IEEE.

Yan, Z., & Wang, J. (2012). Model predictive control of nonlinear systems with unmodeled dynamics based on feedforward and recurrent neural networks. *IEEE Transactions on Industrial Informatics*, *8*(4), 746-756. https://doi.org/10.1109/TII.2012.2205582

Yang, H., Yu, Y., Yuan, Y., & Fan, X. (2015). Backstepping control of two-link flexible manipulator based on an extended state observer. *Advances in Space Research*, *56*(10), 2312-2322, https://doi.org/10.1016/j.asr.2015.07.036

Zain, B. A. M., Tokhi, M. O., & Toha, S. F. (2009). PIDbased control of a single-link flexible manipulator in vertical motion with genetic optimisation. In *Computer Modeling and Simulation, 2009. EMS'09. Third UKSim European Symposium on*, (pp. 355-360). IEEE. https://doi.org/10.1109/EMS.2009.86

Zebin, T. & Alam, M. (2012). Modeling and control of a two-link flexible manipulator using fuzzy logic and genetic optimization techniques. *Journal of Computers*, *7*(3), 578-585, https://doi.org/10.4304/jcp.7.3.578-585

Zouari, F., Saad, K. B., & Benrejeb, M. (2013). Adaptive backstepping control for a single-link flexible robot manipulator driven dc motor. *In Control, Decision and Information Technologies (CoDIT), 2013 International Conference on*, (pp. 864-871). IEEE. https://doi.org/10.1109/CoDIT.2013.6689656